catalysts

MDPI

Article

Comparative Assessment of First-Row 3d Transition Metals (Ti-Zn) Supported on CeO_2 Nanorods for CO_2 Hydrogenation

Maria Lykaki [1,*], Sofia Stefa [1,2], Georgios Varvoutis [3], Vassilios D. Binas [2,4], George E. Marnellos [5,6] and Michalis Konsolakis [1,*]

[1] School of Production Engineering and Management, Technical University of Crete, 73100 Chania, Greece; sstefa@tuc.gr
[2] Institute of Electronic Structure and Laser, Foundation for Research and Technology-Hellas (FORTH–IESL), Vasilika Vouton, 71110 Heraklion, Greece; vbinas@chem.auth.gr
[3] Department of Mechanical Engineering, University of Western Macedonia, 50100 Kozani, Greece; gvarvoutis@uowm.gr
[4] School of Chemistry, Faculty of Sciences, Aristotle University of Thessaloniki, 54124 Thessaloniki, Greece
[5] Chemical Process & Energy Resources Institute, Centre for Research & Technology Hellas, 57001 Thessaloniki, Greece; gmarnellos@cheng.auth.gr
[6] School of Chemical Engineering, Faculty of Engineering, Aristotle University of Thessaloniki, 54124 Thessaloniki, Greece
* Correspondence: mlykaki@tuc.gr (M.L.); mkonsolakis@tuc.gr (M.K.)

Abstract: Herein, motivated by the excellent redox properties of rod-shaped ceria (CeO_2-NR), a series of TM/CeO_2 catalysts, employing the first-row 3d transition metals (Ti, V, Cr, Mn, Fe, Co, Ni, Cu, and Zn) as active metal phases, were comparatively assessed under identical synthesis and reaction conditions to decipher the role of active metal in the CO_2 hydrogenation process. Notably, a volcano-type dependence of CO_2 hydrogenation activity/selectivity was disclosed as a function of metal entity revealing a maximum for the Ni-based sample. Ni/CeO_2 is extremely active and fully selective to methane (Y_{CH4} = 90.8% at 350 °C), followed by Co/CeO_2 (Y_{CH4} = 45.2%), whereas the rest of the metals present an inferior performance. No straightforward relationship was disclosed between the CO_2 hydrogenation performance and the textural, structural, and redox properties, whereas, on the other hand, a volcano-shaped trend was established with the relative concentration of oxygen vacancies and partially reduced Ce^{3+} species. The observed trend is also perfectly aligned with the previously reported volcano-type dependence of atomic hydrogen adsorption energy and CO_2 activation as a function of 3d-orbital electron number, revealing the key role of intrinsic electronic features of each metal in conjunction to metal–support interactions.

Keywords: ceria nanorods; 3d transition metals; 3d orbital number; CO_2 methanation; reverse water–gas shift; CO_2 hydrogenation

check for updates

Citation: Lykaki, M.; Stefa, S.; Varvoutis, G.; Binas, V.D.; Marnellos, G.E.; Konsolakis, M. Comparative Assessment of First-Row 3d Transition Metals (Ti-Zn) Supported on CeO_2 Nanorods for CO_2 Hydrogenation. *Catalysts* **2024**, *14*, 611. https://doi.org/10.3390/catal14090611

Academic Editor: Giuseppe Bonura

Received: 7 August 2024
Revised: 10 September 2024
Accepted: 10 September 2024
Published: 11 September 2024

Copyright: © 2024 by the authors. Licensee MDPI, Basel, Switzerland. This article is an open access article distributed under the terms and conditions of the Creative Commons Attribution (CC BY) license (https://creativecommons.org/licenses/by/4.0/).

1. Introduction

Global warming has emerged as a pressing environmental issue due to the observed continuous increase in global temperature of 0.2 °C per decade, which is directly linked to the escalation of greenhouse gas emissions [1,2]. As the concentration of greenhouse gasses in the atmosphere continues to rise, the detrimental impact on the environment is greatly enhanced. Specifically, carbon dioxide (CO_2), which originates mainly from fossil fuel energy sources, is a major contributor to the accumulation of greenhouse gasses. To mitigate greenhouse gas emissions, it is imperative to optimize the utilization of fossil fuels and implement effective Carbon Capture and Utilization (CCU) technologies [1,3,4].

A sustainable CCU strategy involves the reduction of captured CO_2 via its reaction with hydrogen, a process known as CO_2 hydrogenation. This method presents an effective means of valorizing CO_2 emissions and efficiently storing surplus power from

non-intermittent renewable energy sources (such as solar and wind) in the form of "green" hydrogen [5–7]. Coupling a CCU process with a water electrolysis unit producing "green" hydrogen inhibits the release of CO_2 emissions, while at the same time converting CO_2 into an energy carrier, such as synthetic natural gas (SNG), which consists mainly of methane and can be integrated in the present natural gas grid network, thus closing the carbon cycle [8,9]. Under atmospheric pressure conditions, it can be achieved by either the mildly endothermic reverse water–gas shift (rWGS) reaction (Equation (1)), which yields CO, or the highly exothermic methanation reaction, commonly known as the "Sabatier reaction" (Equation (2)), which produces CH_4 [10–12].

$$CO_2 + H_2 \leftrightarrow CO + H_2O, \Delta H = +41.2 \text{ kJ/mol} \quad (1)$$

$$CO_2 + 4H_2 \leftrightarrow CH_4 + 2H_2O, \Delta H = -164.7 \text{ kJ/mol} \quad (2)$$

Extensive research has explored various catalytic systems, often summarized in the literature covering catalysts for reactions like rWGS [13–18] and CO_2 methanation [17,19–23]. Notably, composite catalytic systems involving metals supported on reducible metal oxides (e.g., CeO_2 and ZrO_2) or combinations of them have been extensively studied. Among the investigated oxide materials, ceria (CeO_2) has gained significant attention as a supporting carrier due to its exceptional properties such as oxygen storage capacity, oxygen mobility, strong metal–support interactions, and rapid change between its two oxidation states (Ce^{3+} and Ce^{4+}) [15,24–28]. Although ceria-based noble metals (Ru, Rh, and Pd) have demonstrated excellent catalytic activity, their high cost and limited availability make them less preferable from a techno-economic point of view [29–34]. Therefore, recent efforts have focused on the rational design of cost-efficient and highly active non-noble metal catalysts, with particular emphasis on the 3d transition metals, which can adequately adsorb and activate CO_2 molecules [18,25,35–41]. In this direction, we recently showed that by appropriately adjusting the size and shape of ceria carrier via the use of appropriate synthetic routes, extremely active TMs/CeO_2 catalysts can be obtained for the CO_2 hydrogenation reaction with similar reactivity to that of noble metals [42]. For instance, it was shown that Ni catalysts supported on ceria nanoparticles of rod-like morphology exhibit excellent hydrogenation performance, ascribed mainly to the enhanced redox properties of ceria nanorods in conjunction with the synergistic interactions between nickel and ceria nanoparticles [25,43,44]. On the other hand, Cu/CeO_2 samples demonstrate excellent rWGS performance, revealing the key role of the metal entity in CO_2 adsorption/activation and in turn in activity and selectivity towards CO or CH_4 [12,42].

In the case of the rWGS reaction, two main reaction pathways have been considered, namely the redox and the associative mechanism. In the first case, CO_2 is initially activated via its adsorption on metal sites or oxygen vacancies, followed by the formation of carbonyl species that are finally desorbed as $CO_{(g)}$. On the other hand, during the associative mechanism, the adsorbed CO_2 reacts with H adatoms towards the formation of active intermediate species (such as formates) that finally decompose to CO and H_2O [6,15,16,45–48]. The main difference between the two rWGS reaction mechanisms is whether the dissociated hydrogen atoms engage in the reaction and generate carbon-containing intermediates (e.g., carboxyls and formates) with the adsorbed CO_2 on the catalyst surface [15,49,50]. Similarly, the CO and formate-mediated routes have been proposed for CH_4 production. In the first route, the chemisorbed CO derived by CO_2 dissociation is further hydrogenated to CH_4, whereas, in the second one, formate species (HCOO*) react with hydrogen adatoms [51–53]. In view of these aspects, CO_2 dissociation is considered a key step in the overall reaction process, affected to a great extent by the electronic nature of active sites and the charge transfer to CO_2 molecule [47,51,52].

In view of the above discussion, various transition metals have been studied in the context of CO_2 hydrogenation reactions. Remarkably, the first-row transition metals have shown a capacity to adsorb and activate CO_2 by facilitating charge transfer from the metal phase to the CO_2 molecule [40,54]. Furthermore, computational studies have played a crucial role in enhancing our comprehension of the structural aspects and energetic

characteristics of the interplay between metal surfaces and CO_2 chemistry. To this end, Ray and Deo [55] have proposed the local d-density of states (d-DOS) at the Fermi level of the pristine surface as a potential descriptor for CO_2 methanation over alumina-supported Ni and Ni-based alloy catalysts. In particular, the catalytic activity was linearly correlated with the number of electronic excitations from occupied to unoccupied states at the lowest energy cost [55], with this electronic property demonstrating the surface's ability to react to an outside perturbation (e.g., a reactant present above the surface) by displaying a population of unoccupied states [56,57]. Density functional theory (DFT) studies reveal that metals with less than 2 empty 3d orbitals exhibit a unique CO_2 hydrogenation selectivity, favoring formate formation via a specific co-adsorption configuration of a hydrogen atom and CO_2 [58]. In particular, a "volcano" curve on barrier energy in the formate pathway was established with Ni being located at the peak with the lowest barrier energy [58].

Despite the intense interest in the field, there is no—to the best of our knowledge—systematic experimental work on the impact of 3d transition metals on the key activity descriptors and in turn on the CO_2 hydrogenation performance under identical synthesis and catalytic evaluation conditions. The latter could bypass the variability of the synthesis procedure and reaction conditions followed in the relevant literature, revealing solely the role of the metal entity. In this regard, a series of TM/CeO_2 catalysts with a constant atomic ratio of M/Ce = 0.25 were prepared, using the first-row 3d transition metals (Ti, V, Cr, Mn, Fe, Co, Ni, Cu, and Zn) as active phases for ceria nanorods (CeO_2-NR). The catalytic materials were thoroughly characterized in terms of their textural (N_2 adsorption at –196 °C), structural (X-ray diffraction, XRD), morphological (Scanning electron microscopy/Energy dispersive spectroscopy, SEM/EDS, Transmission electron microscopy, TEM), surface (X-ray photoelectron spectroscopy, XPS) and redox (Temperature-programmed reduction, H_2-TPR) properties in an attempt to gain insight into the role of metal entity in CO_2 hydrogenation. Notably, no particular correlation was disclosed between the aforementioned textural, structural, and redox properties and the catalytic performance. However, based on the XPS analysis, a volcano-shaped trend among the relative concentration of oxygen vacancies, the amount of Ce^{3+} species, and the CO_2 conversion rate and CH_4 selectivity were established. Moreover, a volcano-type dependence of both activity and selectivity as a function of 3d-orbital electron number was disclosed, with Ni located at the peak of the volcano curve. These findings can be interpreted on the basis of the intrinsic electronic features of each metal in relation to their ability to activate CO_2 and dissociate H_2, in compliance with relevant theoretical studies.

2. Results

2.1. Textural and Structural Characterization (BET (Brunauer–Emmett–Teller), XRD)

The main textural and structural characteristics of bare CeO_2-NR and TM/CeO_2 samples (atomic ratio M/Ce = 0.25) are summarized in Table 1. Bare CeO_2 demonstrates a BET surface area of 79 m^2/g while a slight decrease in the BET surface area is observed upon the addition of the transition metals into ceria support.

XRD patterns of bare CeO_2-NR and TM/CeO_2 samples are presented in Figure 1. The main diffraction peaks of bare CeO_2 correspond to the following planes: (111), (200), (220), (311), (222), (400), (331), and (420) and are attributed to the face-centered cubic (fcc) fluorite structure of ceria (Fm3m symmetry, no. 225) [59,60]. Furthermore, in the case of TM/CeO_2 samples (M: Ti, Fe, Co, Ni, Cu, and Zn), smaller peaks of their corresponding oxides are detected, demonstrating the existence of TiO_2, Fe_2O_3, Co_3O_4, NiO, CuO, and ZnO, respectively, with no other crystal phases existing, apart from ceria. In contrast, Mn/CeO_2 and Cr/CeO_2 samples do not present any diffraction peaks, except from the ceria crystal phase, a fact that can be attributed to the low metal loadings in conjunction with the high metal dispersion, rendering the calculation of their crystallite sizes impossible. In the XRD pattern of V/CeO_2, apart from ceria characteristic peaks, a series of XRD peaks located at 2θ values around 18.2°, 24.0°, 32.4°, 34.2°, 39.0°, 43.5°, 46.4°, 47.9°, 49.2°, 55.5°, and 60.2° were observed, which are related to the (101), (200), (112), (220), (301), (103), (321), (312), (400), (420) and (332) planes of $CeVO_4$ [61,62], respectively. Therefore, it is evident

that in the case of V/CeO_2, a mixed crystal phase has been formed via the impregnation method, including CeO_2 and $CeVO_4$.

Table 1. Textural and structural characteristics of CeO_2 and TM/CeO_2 samples.

Sample	Nominal Metal Loading	EDS Analysis		BET Analysis	XRD Analysis		TEM Analysis
		Atomic Ratio M/Ce	Metal Content (wt%)	S_{BET} (m^2/g)	Average Crystallite Size (nm)		M_xO_y Particle Size (nm)
					CeO_2	M_xO_y	
CeO_2-NR	-	-	-	79	15	-	-
Ti/CeO_2	6.5	0.24	6.3	-	11	20	16
V/CeO_2	6.9	0.28	7.6	-	14	45	28
Cr/CeO_2	7.0	0.26	7.2	-	11	- [1]	10
Mn/CeO_2	7.4	0.22	6.5	-	11	- [1]	15
Fe/CeO_2	7.5	0.21	6.3	69	10	7	11
Co/CeO_2	7.9	0.26	8.1	72	14	16	15
Ni/CeO_2	7.9	0.25	7.8	72	14	23	10
Cu/CeO_2	8.5	0.25	8.6	75	12	43	16
Zn/CeO_2	8.7	0.24	8.3	76	12	44	41

[1] Not calculated due to the absence of the corresponding XRD peaks.

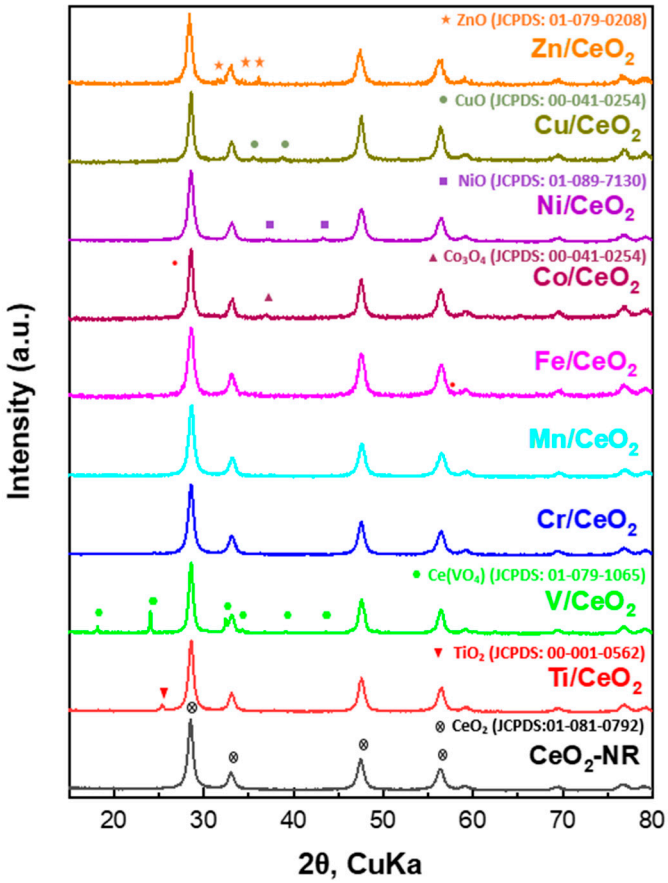


Figure 1. XRD patterns of CeO_2-NR and TM/CeO_2 samples.

The average crystallite sizes of CeO_2 and M_xO_y phases for both bare ceria and TM/Ceria samples are calculated by Scherrer's equation (Equation (4)) and are presented in Table 1. The crystallite size of ceria does not significantly change with the impregnation of the metal entity (11–15 nm), indicating that ceria structural properties remain unaltered upon metal addition. The crystallite sizes of the active metal phases are following the order: $CeVO_4$ (45 nm) > ZnO (44 nm) > CuO (43 nm) > NiO (23 nm) > TiO_2 (20 nm) > Co_3O_4 (16 nm) > Fe_2O_3 (7 nm).

2.2. Morphological Characterization (SEM/TEM)-Elemental Analysis (SEM/EDS)

Elemental analysis was performed by SEM along with energy dispersive X-ray spectrometry (SEM/EDS) on the TM/CeO_2 samples and the results (atomic ratio of M/Ce, metal content in weight percentage) are presented in Table 1. The atomic ratio of M/Ce is in good agreement with the nominal one. Additionally, the SEM images of the TM/CeO_2 samples are depicted in Figure 2. From SEM/EDS analysis, it is revealed that there is a uniform distribution of ceria and metal phases on the entire surface of the mixed oxides.

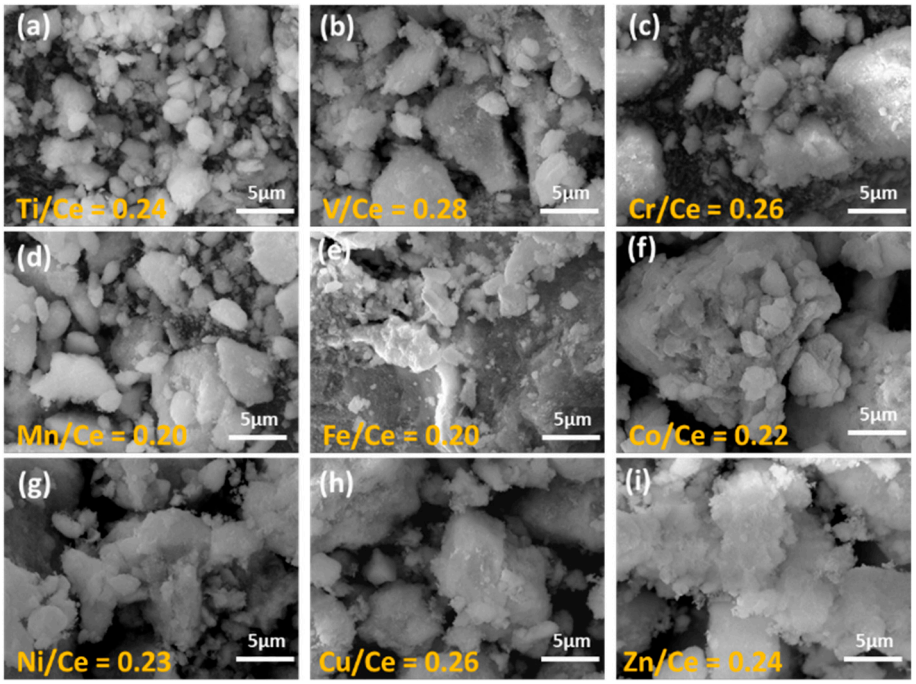


Figure 2. SEM images of the samples: (**a**) Ti/CeO_2, (**b**) V/CeO_2, (**c**) Cr/CeO_2, (**d**) Mn/CeO_2, (**e**) Fe/CeO_2, (**f**) Co/CeO_2, (**g**) Ni/CeO_2, (**h**) Cu/CeO_2 and (**i**) Zn/CeO_2.

The morphological characteristics of all samples were investigated in more detail by TEM analysis, as shown in Figure 3. It is apparent that CeO_2 support retains its nanorod morphology upon the addition of the metal entity, with isolated M_xO_y particles of irregular shape being detected in all TM/CeO_2 samples. Moreover, the M_xO_y particle sizes (Table 1), along with the particle size distribution (Figure 3) were determined by TEM analysis. M_xO_y particle size varied widely, ranging between 10 and 41 nm (Table 1).

2.3. Reducibility Studies (H_2-TPR)

In order to gain insight into the impact of the metal entity on the reducibility, TPR measurements were performed in the temperature range of 100–1000 °C, using H_2 as a reducing agent. More particularly, indicative catalytic systems (vide infra), in terms of conversion and selectivity, were chosen for the reducibility studies, namely, the Ni/CeO_2 and Co/CeO_2 catalysts, as highly active for the Sabatier reaction and the Fe/CeO_2 and Cu/CeO_2 ones, as representatives for the rWGS reaction. As depicted in Figure 4, bare CeO_2-NR exhibits two broad reduction peaks centered at 545 °C and 788 °C which are attributed to the surface (O_s) and bulk (O_b) oxygen reduction in ceria, respectively [63,64]. The Fe/CeO_2 sample exhibits four reduction peaks at 390 °C, 465 °C, 588 °C, and 759 °C with the peaks at 465 °C and 759 °C being ascribed to ceria surface oxygen and bulk oxygen reduction, respectively, while the peaks at 390 °C and 588 °C corresponding to the reduction in the iron species, namely Fe_2O_3 to Fe_3O_4 and Fe_3O_4 to Fe^0 [65]. As for the Co/CeO_2 sample, it exhibits two main reduction peaks at 318 °C and 388 °C, ascribed to the stepwise reduction of Co_3O_4 to CoO and CoO to metallic Co, respectively [66]. Concerning the Cu/CeO_2 sample, the low-temperature peak at 181 °C is attributed to the reduction of finely

dispersed CuO_x species strongly interacting with the ceria surface, while the peak at 217 °C can be ascribed to the reduction of Cu_2O to Cu^0 due to the interaction of the Cu–[O_x]–Ce structure [67–69]. Nickel–ceria nanorods exhibit three peaks; the peak at 220 °C can be attributed to the reduction of surface oxygen located at the defects of the ceria surface, the peak at 288 °C corresponds to the reduction of adsorbed oxygen species associated with the formation of Ni–O–Ce structure, while the peak at 353 °C is ascribed to the reduction of the well-dispersed NiO phase interacting strongly with the ceria support [70,71]. All TM/CeO_2 samples exhibit a high-temperature peak in the range of 747–793 °C which is attributed to the ceria sub-surface oxygen reduction. As illustrated in Figure 4, the addition of the metal phase facilitates ceria surface oxygen reduction.

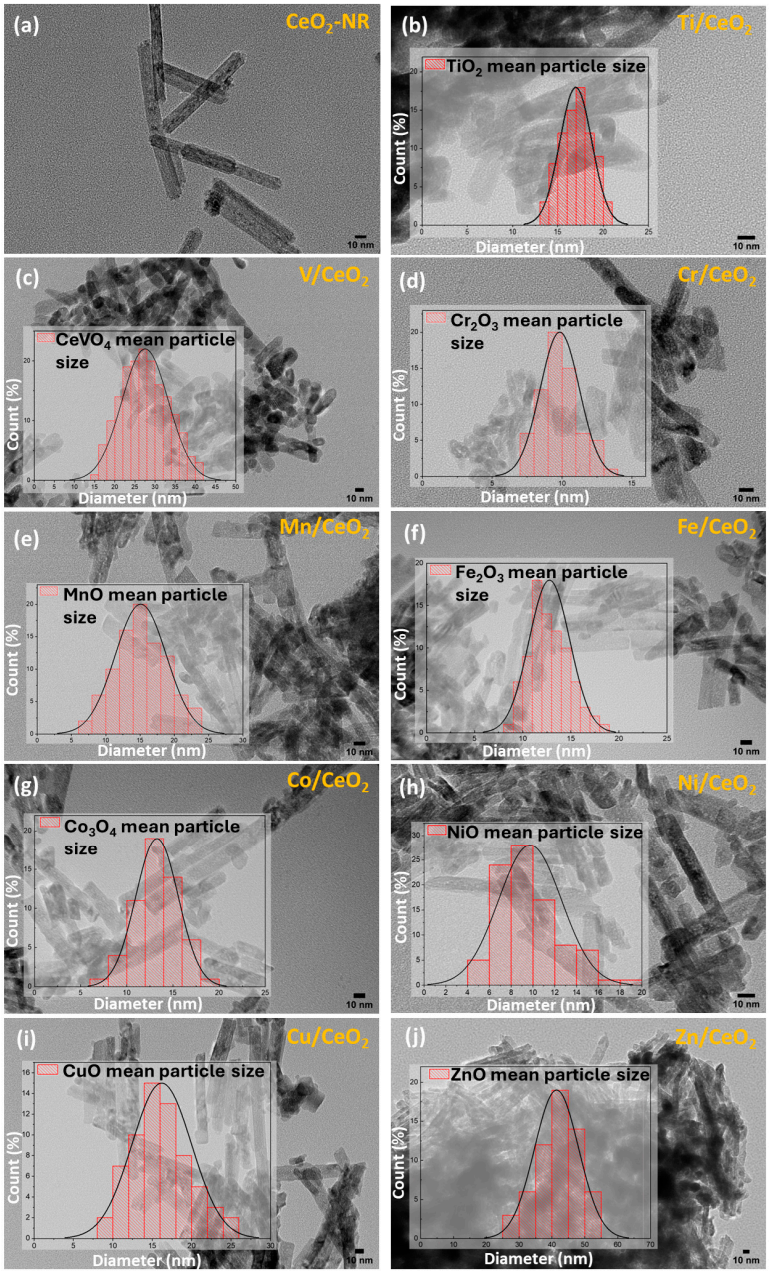


Figure 3. TEM images of the samples: (**a**) CeO_2-NR, (**b**) Ti/CeO_2, (**c**) V/CeO_2, (**d**) Cr/CeO_2, (**e**) Mn/CeO_2, (**f**) Fe/CeO_2, (**g**) Co/CeO_2, (**h**) Ni/CeO_2, (**i**) Cu/CeO_2 and (**j**) Zn/CeO_2.

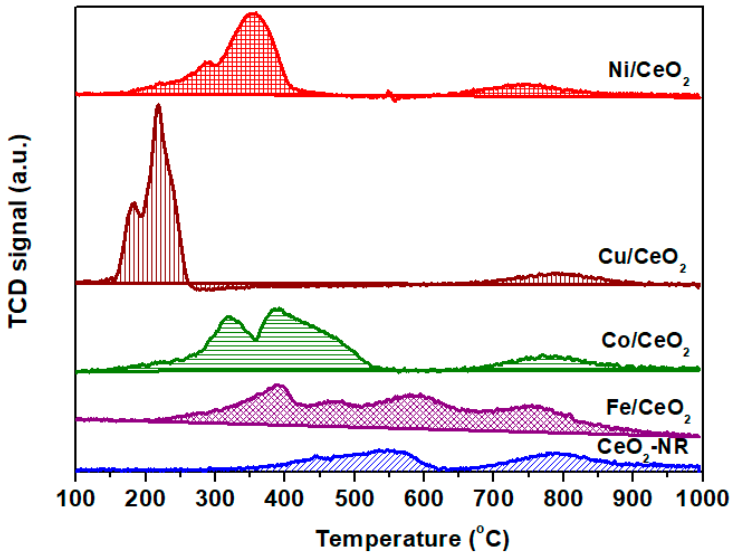


Figure 4. H_2-TPR profiles of CeO_2-NR and representative TM/CeO_2 samples.

Furthermore, as depicted in Table 2, hydrogen consumption surpasses the theoretical amount for all TM/CeO_2 samples, apart from the Fe/CeO_2 sample, revealing that the addition of the metallic phase enhances the reducibility of ceria nanorods, due to synergistic metal–support interactions.

Table 2. Redox properties of CeO_2-NR and representative TM/CeO_2 samples.

Sample	H_2 Consumption (mmol H_2 g^{-1}) [1]	Theoretical H_2 Consumption (mmol H_2 g^{-1}) [2]	Peak Temperature (°C)			
CeO_2-NR	0.6	-	-	545	-	788
Fe/CeO_2	1.6	1.9	390	465	588	759
Cu/CeO_2	1.8	1.3	181	-	217	793
Ni/CeO_2	1.8	1.3	220	288	353	747
Co/CeO_2	2.4	1.7	318	-	388	789

[1] Estimated by the area of the corresponding TPR peaks, which is calibrated against a known amount of CuO standard sample. [2] Calculated as the amount of H_2 required for the complete reduction in fully oxidized M_xO_y to M^0 on the basis of the metal nominal loading.

2.4. Surface Analysis (XPS)

In order to assess the impact of surface chemistry on the intrinsic properties and catalytic performance, XPS analysis was conducted over the optimum catalytic materials (TM/CeO_2, TM: Fe, Cu, Co, Ni) in their reduced states. In Figure 5a, the Ce 3d XPS spectra are depicted with the Ce $3d_{3/2}$ and Ce $3d_{5/2}$ states corresponding to the u and v lines, respectively. The three pairs of peaks u (902.1 eV), u″ (908.5 eV), u‴ (917.3 eV) and v (883.2 eV), v″ (889.8 eV), v‴ (899.5 eV) characterize the Ce^{4+} species, while the u′ (904.7 eV) and v′ (886.2 eV) peaks are attributed to the Ce^{3+} species [72–74].

The concentration of Ce^{3+} species can be calculated from the following equation (Equation (3)) [72]:

$$\left[Ce^{3+}\right] = \frac{Ce(III)}{Ce(III) + Ce(IV)} \quad (3)$$

where Ce(III) and Ce(IV) denote the corresponding sums of the integrated peak areas associated with the Ce^{3+} and Ce^{4+} XPS signals, respectively (Table 3). Ni catalyst exhibits the highest amount of Ce^{3+} species (30.4%), followed by Co (29.9%), Fe (26.9%) and Cu (25.5%). The significant role of Ce^{3+} species in the CO_2 hydrogenation process (activation of CO_2 and formation of active intermediates) has been revealed in the literature [75–77], with these sites being associated with the abundance of oxygen vacancies and the extent of metal–support interactions [78]. Cao et al. [79] demonstrated a volcano-type curve between activity and

surface Ce^{3+} fractions for CO_2 hydrogenation to CO over ceria catalysts. Moreover, under CO_2 hydrogenation reaction conditions, a Ni catalyst supported on mesoporous ceria nanofiber assembly was found to lead to the formation of active Ce^{3+} sites located at the interface, thus boosting the catalytic performance and promoting the formate pathways [80].

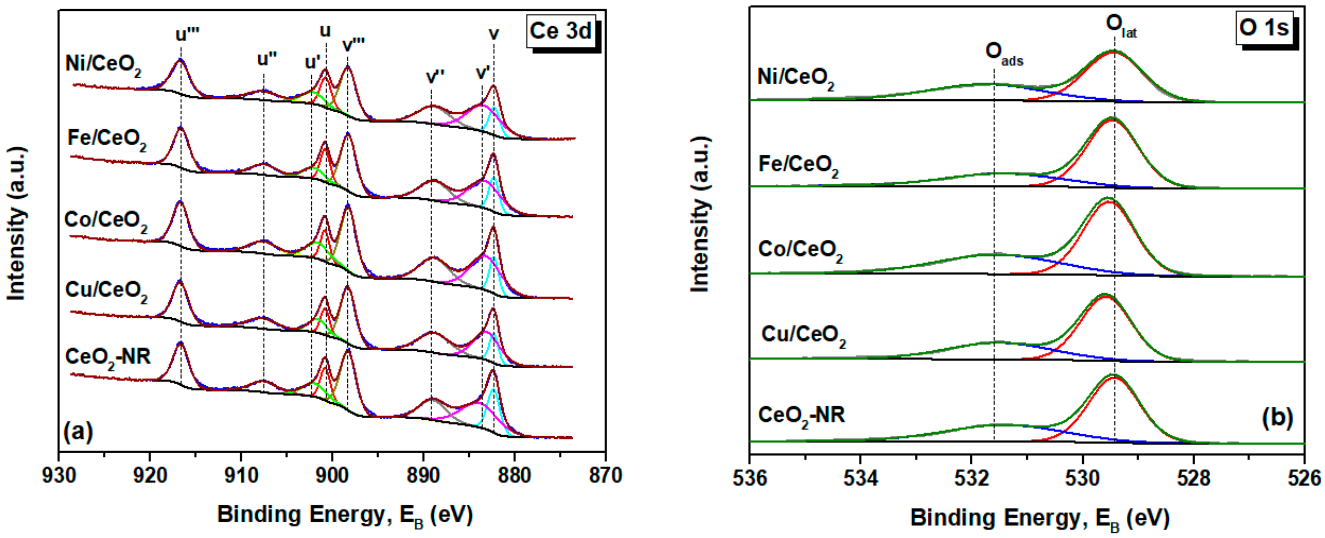


Figure 5. XPS spectra of (**a**) Ce 3d and (**b**) O 1s of the reduced CeO_2-NR and optimum catalysts (Fe, Co, Ni, Cu).

Table 3. XPS results of representative reduced samples.

Sample	O_{ads}/O_{lat}	Ce^{3+} (%)
CeO_2-NR	0.59	27.2
Fe/CeO_2	0.43	26.9
Cu/CeO_2	0.54	25.5
Co/CeO_2	0.63	29.9
Ni/CeO_2	0.65	30.4

Figure 5b illustrates the O 1s XPS spectra with two peaks being observed; the peak at 529 eV represents the lattice oxygen (O_{lat}), while the peak at 531 eV is ascribed to surface adsorbed oxygen species (O_{ads}) [81,82]. Analysis of the O 1s XPS spectra of the reduced samples led to the determination of the O_{ads}/O_{lat} ratio which constitutes a useful tool for the estimation of the relative oxygen vacancy concentration [54,81]. As shown in Table 3, the Ni catalyst presents the highest O_{ads}/O_{lat} ratio, with the following order being observed: $Ni/CeO_2 > Co/CeO_2 > Cu/CeO_2 > Fe/CeO_2$, in good agreement with the order of Ce^{3+} species (Table 3).

Figure 6a presents the Cu 2p XPS spectrum of the reduced Cu/CeO_2 catalyst which includes two main peaks at 953.7 eV and 933.8 eV, ascribed to Cu $2p_{1/2}$ and Cu $2p_{3/2}$ states, respectively. The existence of satellite peaks at 943 and 962 eV confirms the presence of Cu^{2+} species [69,83]. The Co 2p XPS spectrum for the reduced Co/CeO_2 sample (Figure 6b) exhibits two main peaks of Co $2p_{1/2}$ (796.6 eV) and Co $2p_{3/2}$ (780.6 eV), as well as shake-up satellites at 786 eV which are characteristics of Co^{2+} [84,85]. Moreover, Figure 6c depicts the Fe 2p XPS spectrum of the reduced Fe/CeO_2 catalyst. There are two peaks at 711 and 724 eV, assigned to the Fe $2p_{3/2}$ and Fe $2p_{1/2}$, respectively, and two satellite peaks at 719 and 734 eV, designating the presence of Fe^{3+} [86,87]. The satellite peaks overlap with the Auger Ce MNN peaks. The formation of Fe^{2+} species results from the iron oxide–ceria interaction via an interfacial redox process: $xFe_2O_3 + (2 - y)CeO_{2-x} \rightarrow xFe_2O_{3-y} + (2 - y)CeO_2$ [86,88,89]. In addition, Figure 6d illustrates the Ni 2p XPS spectrum of the reduced Ni/CeO_2 sample, with two peaks at 855 eV (Ni $2p_{3/2}$) and at 873 eV (Ni $2p_{1/2}$), along with a broad satellite peak at 861 eV, associated

with the presence of Ni^{3+} species (Ni_2O_3) [90,91]. According to the XPS results of the reduced catalysts, metal species exist in different oxidation states which can be related to the strength of the metal–support interactions, as indicated in the literature [85,90]. Nevertheless, the difficulty in establishing reliable relationships between metal oxidation states and catalytic performance should be underscored, on the ground of ex situ nature of XPS in conjunction with different metal entities employed as active phases in the present work.

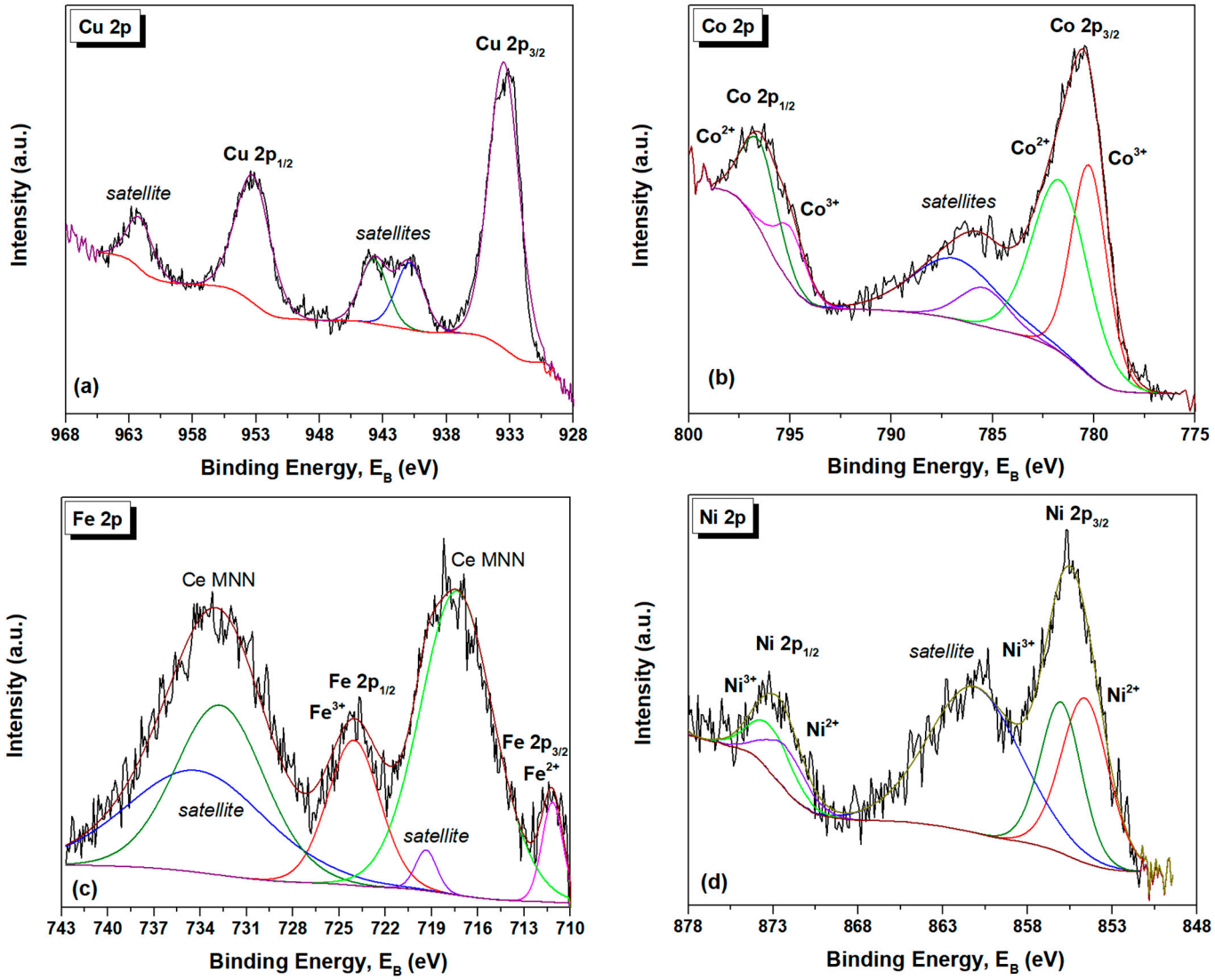


Figure 6. XPS spectra of (**a**) Cu 2p, (**b**) Co 2p, (**c**) Fe 2p, and (**d**) Ni 2p of the reduced optimum catalysts (Fe, Co, Ni, Cu).

2.5. Catalytic Performance

Figure 7 depicts the CO_2 conversion and CO selectivity performance in the temperature range of 200–500 °C of all TM/CeO_2 samples. For comparison purposes, the corresponding performance of bare ceria nanorods is also included. The main conclusions that can be drawn by the comparative assessment of the first-row 3d transition metals supported on CeO_2 nanorods are the following:

(i) The CO_2 conversion of TM/CeO_2 is strongly dependent on the metal entity, following the general trend: Ni > Co > Cu > Fe > Zn > Cr ≈ Ti ≈ V ≈ Mn.

(ii) The Ni/CeO_2 catalyst exhibits by far the best performance overall, in terms of maximum conversion and light-off temperature, offering ~90% conversion at 300 °C, which is close to equilibrium conversion (94%) under the employed experimental condi-

tions. Equally importantly, Cu/CeO_2 was the most active rWGS material, attaining a CO_2-to-CO conversion of 47% at 450 °C, approaching equilibrium conversion (48.5%).

(iii) The early 3d transition metals (Ti, V, Cr, Mn) are almost inactive (i.e., X_{CO2} < 10% at T < 400 °C), exhibiting an even lower conversion performance as compared to bare ceria nanorods.

(iv) All TM/CeO_2 systems, except for Ni and Co, are mainly selective to CO. In particular, the Ni-based catalyst is completely selective to CH_4 in the whole temperature range investigated, whereas the Co-based sample exhibits intermediate selectivity values depending on temperature. All other TM/CeO_2 catalysts are completely selective to CO.

(v) In terms of CO_2 conversion and CO/CH_4 selectivity, no catalyst deactivation occurred during short-term (24 h) stability experiments over the optimum catalysts (Fe, Co, Ni, Cu) supported on ceria nanorods (not shown for brevity).

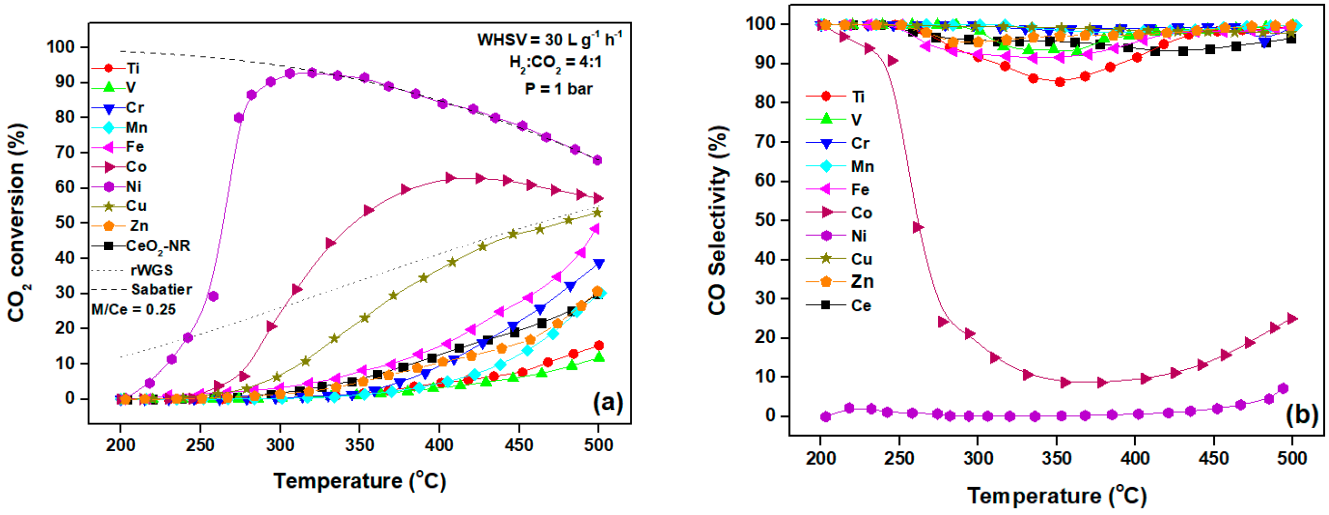


Figure 7. Comparative assessment of (**a**) CO_2 conversion and (**b**) selectivity to CO for the first-row 3d transition metals supported on CeO_2 nanorods. Reaction conditions: WHSV = 30 $L \cdot g^{-1} \cdot h^{-1}$, $H_2:CO_2$ = 4, P = 1 bar.

In order to gain a more thorough insight into the particular role of the metal entity in CO_2 hydrogenation performance, the normalized reaction rate of CO_2 consumption (r_{CO2}) and the corresponding selectivity to methane (S_{CH4}) are plotted at a specific reaction temperature (350 °C), as at this temperature noticeable differences can be unveiled among the samples (Figure 8). Markedly, a volcano-type dependence of CO_2 conversion and CH_4 selectivity was disclosed for first-row 3d transition metals, i.e., Ti, V, Cr, Mn, Fe, Co, Ni, Cu, Zn with a maximum obtained for Ni. In particular, the Ni/CeO_2 catalyst exhibits by far the optimum hydrogenation performance in terms of CO_2 consumption rate (~800 μmol $g_{Ni}^{-1}s^{-1}$) and CH_4 selectivity (100%), followed by Co (r_{CO2} = 445 μmol $g_{Co}^{-1}s^{-1}$, S_{CH4} = 90%). The 3d early transition metals (Ti–Fe), as well as the 3d late metals (Cu and Zn), exhibit much lower reactivity (r_{CO2} < 200 μmol $g_M^{-1}s^{-1}$), while being selective to CO (Figure 8).

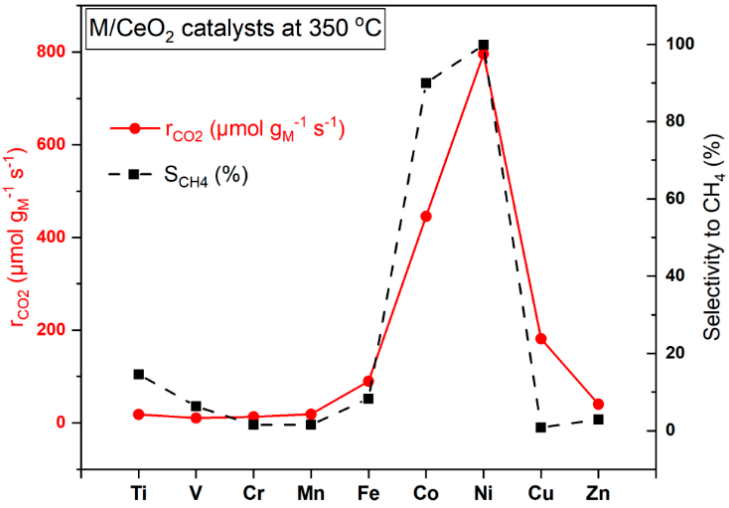


Figure 8. Metal entity-dependence of CO_2 conversion (solid line) and CH_4 selectivity (dashed line) at 350 °C for the first-row 3d transition metals supported on CeO_2 nanorods.

3. Discussion

In the present study, the CO_2 hydrogenation performance of first-row 3d transition metals (Ti–Zn) supported on CeO_2 nanorods (atomic ratio M/Ce = 0.25) were comparatively assessed employing identical synthesis and catalytic evaluation procedures, in an attempt to decipher the role of metal entity and metal–support interactions in the catalytic activity and selectivity. The as-prepared samples were characterized by various physicochemical methods to gain insight into the impact of metal nature on the structural, textural, morphological, and redox properties. On the basis of the obtained results, it could be argued that Ni/CeO_2—and to a lower extent Co/CeO_2—is active for the Sabatier reaction, whereas the rest of the transition metals exhibit a much inferior reactivity while being selective to CO (rWGS). Remarkably, a volcano-type dependence of CO_2 hydrogenation activity and selectivity was disclosed as a function of metal entity (Ti–Zn) revealing a maximum for the Ni-based sample. In particular, Ni/CeO_2 is highly active and fully selective to CH_4 (Y_{CH4} = 90.8% at 350 °C), followed by Co (Y_{CH4} = 45.2% at 350 °C). The rest of the transition metals exhibit a much lower CO_2 conversion, being also selective to CO instead of CH_4. In an attempt to disclose possible structure-performance relationships and to reveal key activity descriptors, the obtained catalytic findings are discussed below in relation to the present characterization results and the intrinsic characteristics of each metal, taking into account the main reaction pathways suggested for Sabatier and rWGS reactions.

Firstly, the rWGS and Sabatier reaction mechanisms are considered, both constituting a topic of intensive debate. For the rWGS reaction, two main pathways have been in general considered, i.e., the redox and the associative mechanism, depending on the direct or not participation of H_2 in CO_2 activation [47,48]. In the redox mechanism, the gaseous CO_2 is initially activated via its adsorption on an electron donor site, such as a metal or oxygen vacancy, followed by the formation of carbonyl species that are finally desorbed as $CO_{(g)}$. In this specific route, the role of H_2 is limited to reducing the oxidized sites and sustaining the reduction/oxidation cycle on the catalyst surface [6,49]. Conversely, within the associative mechanism, CO_2 chemisorbed species react with H adatoms derived from H_2 dissociation for the formation of intermediate species (such as formates) that eventually decompose to CO and H_2O [6,13,41].

Similarly, two main paths have been proposed for CO_2 methanation, i.e., the CO and formate route. The former is related to the dissociation of $CO_{2(g)}$ to $CO_{(ad)}$ which is fully hydrogenated to $CH_{4(ad)}$ [51,52]. In the second route, formate species (HCOO*) instead of CO is the main intermediate, followed by a reaction with chemisorbed hydrogen adatoms [51,52,92]. With regard to the role of metal–ceria catalysts in the mechanism of hydrogen activation, it is considered that gas-phase H_2 is activated via dissociation on metal

particles that are increasingly active towards hydrogen activation in the vicinity of ceria surfaces. The adsorbed hydrogen adatoms rapidly migrate to the ceria support via spillover phenomena and can react with low-energy and abundant C-containing intermediates onto CeO_{2-x} and result in gaseous methane molecules [93]. In this regard, in situ DRIFT experiments have revealed the involvement of the direct formate hydrogenation pathway in CO_2 methanation over a nickel–ceria catalyst prepared via sol–gel, with this synthetic procedure promoting oxygen vacancy formation and exposure of the Ni (111) crystal plane [94].

In principle, the CO_2 activation pathway is strongly affected by the metal entity and metal–oxygen interaction [95]. In this regard, it has also been found that the adsorption strength of CO_2 on metal surfaces is affected by the electronic nature of active sites, i.e., the d-band center of the metal as well as the charge transfer to a CO_2 molecule [96]. According to the d-band center model, the adsorption energy of a given molecule can uniformly decrease (increase) from one transition metal surface to another in which the d-electron number increases (decreases). Nevertheless, exceptions from the model can occur possibly due to the adsorbate's large electronegativity and/or the substrate's nearly full d-band [97].

Moreover, it is considered that M–CO bond strength determines the selectivity of CO_2 hydrogenation to either CO or CH_4; weak interaction results in the desorption of CO as a final product, whereas strong interaction facilitates its further hydrogenation to CH_4. In this regard, it has been found via computational studies that the CO adsorption energy can be considered as a selectivity descriptor [6]. In specific, metal atoms with high CO desorption energy (such as Pd, Pt, Ni, and Rh) tend to mainly catalyze the methanation reaction, whereas group 11 metals (Cu, Ag, Au) with lower CO desorption energy produce CO as the main product. These findings are in complete agreement with the present ones (Figure 8), revealing the key role of metal nature in CO_2 activation.

In light of the above discussion, CO_2 activation in conjunction with H_2 dissociation on metal sites could be considered as the main factors determining activity and selectivity. In view of this fact, in a comprehensive work, Sun et al. [58] theoretically explored 3d transition metals in relation to their activity and selectivity in CO_2 hydrogenation by taking into account the adsorption configurations of H_2, CO_2, and the co-adsorption of H atom and CO_2 on metal sites. In Figure 9, adopted from the aforementioned article, the atomic hydrogen adsorption energy (Figure 9a), the barrier energy (Figure 9b), and the CO_2 charge change (Figure 9c) are depicted as functions of 3d-orbital electron transfer during the CO_2 hydrogenation.

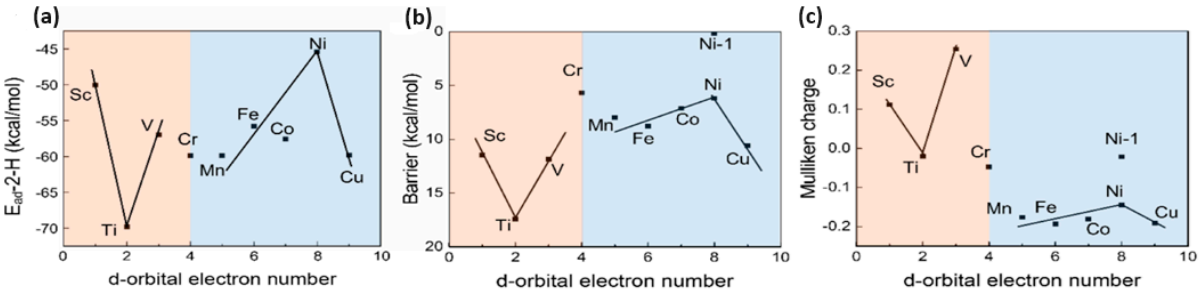


Figure 9. (**a**) Atomic H adsorption energy on P-2,5-DCP-CTF-M-CO2 ((2-pyridyl)-s-triazine is the simplified unit model of the covalent triazine frameworks (CTF), the unit model and its metal complex is P-2,5-DCP-CTF-M (M = Sc, Ti, V, Cr, Mn, Fe, Co, Ni, Cu, Zn)), (**b**) barrier energy, and (**c**) change in CO_2 charge from IS to TS (C) in the formate pathway as a function of 3d-orbital electron number. Initial state (IS) of CO_2 hydrogenation corresponding to the co-adsorption configuration of CO_2 and H atom on the active metal site; transition states (TS); Sc, Ti, and V atoms with less than four 3d-orbital electrons were divided in the left region (orange). The metal atoms, including Mn, Fe, Co, Ni, and Cu, having more than four 3d-orbital electrons were divided in the right region (blue). Reproduced with permission from [58].

It is evident that there is a volcano-type dependence of barrier energy in relation to the number of 3d-orbital electrons, with Ni located at the peak with the lowest energy. This implies the superiority of Ni for CO_2 hydrogenation among the other 3d metals. Moreover, the change in charge from IS (initial state) to TS (transition states) on adsorbed CO_2 also exhibits a volcano-shaped relationship in agreement with the barrier energy, confirming that the barrier energy is closely correlated to electron transfer. Besides, the adsorption energy of H atoms is perfectly correlated with the barrier energy of CO_2 hydrogenation, being again the lowest for Ni [58].

Notably, a perfect agreement between the theoretically predicted trend for CO_2 hydrogenation via the formate pathway (Figure 9) and the present experimental findings over supported catalysts (Figure 8) was revealed for the first time, implying the key role of the energy barrier for CO_2 activation and H_2 dissociation. In other words, the intrinsic characteristics of each metal related to the d-band center and the charge transfer to CO_2 or H_2 molecules can be considered as the main factors, affecting the activation of CO_2 and its consequent hydrogenation to methane or other products.

The above is further supported by the lack of straightforward relationships between the structural and redox properties of TM/CeO_2 samples explored in the present work. In specific, the majority of TM/CeO_2 samples exhibit similar textural and structural properties (Table 1), despite their widely separated catalytic performance. Moreover, both the metal and ceria crystallite sizes are not affected, to a great extent, by metal entities, suggesting similar interfacial interactions. For instance, although Ni, Co, and Cu possess similar surface areas (72–75 m^2/g) and crystallite sizes for ceria support (12–14 nm) and metal active phase (10–16 nm), they exhibit completely different performance, in terms of activity and selectivity. Similarly, taking into account the present H_2-TPR results, it can be inferred that the reducibility cannot be considered by itself as the key activity/selectivity descriptor during the CO_2 hydrogenation process. In other words, the differences in the redox behavior, in terms of H_2 uptake and TPR peak temperatures (Table 2), cannot be solely accounted for the dissimilar hydrogenation performance of explored samples.

However, taking into account the XPS results, it is noteworthy that a volcano-shaped trend was revealed among the oxygen vacancy and Ce^{3+} species concentrations and the CO_2 conversion rate and CH_4 selectivity at 350 °C for the optimum rod-shaped reduced catalysts (Fe, Cu, Co, and Ni), following the order: Fe/CeO_2 < Cu/CeO_2 < Co/CeO_2 < Ni/CeO_2 (Figure 10).

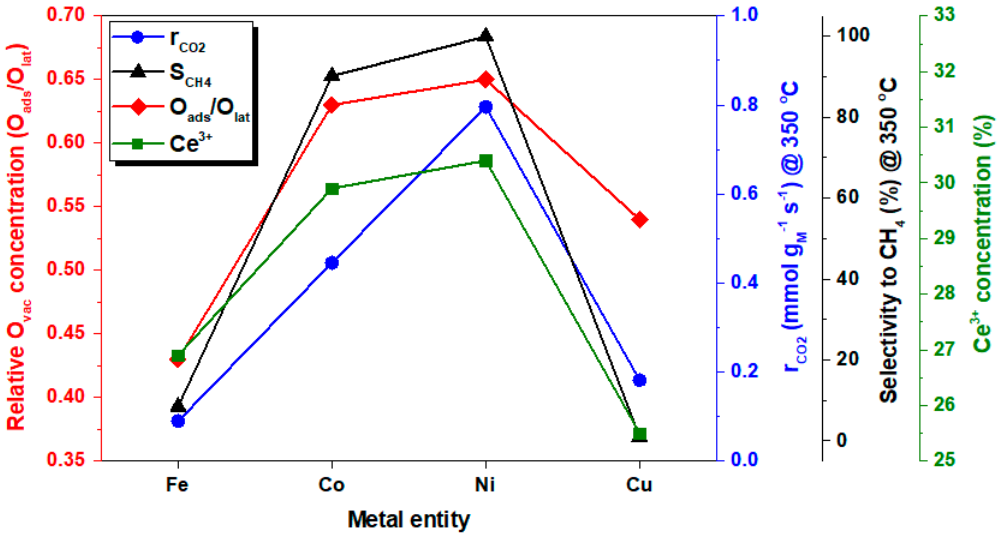


Figure 10. Relationship among the CO_2 conversion rate and CH_4 selectivity at 350 °C with the relative oxygen vacancy and Ce^{3+} concentrations for the optimum reduced catalysts (Fe, Co, Ni, Cu).

These results clearly demonstrate the fundamental role of the metal entity and in turn of metal–support interactions towards determining the relative abundance of oxygen vacancies and partially reduced cerium species, both essential for CO_2 activation. In particular, Lee et al. [98] proposed that Ce^{3+} sites with oxygen vacancies over nickel–ceria catalyst led to the activation of CO_2 towards the formation of carbonate species that are hydrogenated to formate and finally to methane. In a similar manner, nickel–ceria nanorods exhibited higher methanation activity than their nanocubes counterparts in the low-temperature range (200–250 °C) due to their abundance in oxygen vacancies which have a direct effect on the formation of active intermediates [36]. The {110} facets mainly exposed on ceria nanorods have the ability to generate and stabilize the oxygen vacancy sites which are essential in CO_2 to CH_4 conversion [99]. Nevertheless, the pivotal role of metal–support interactions in catalytic activity should be underscored, as the experimental results of the present study clearly reveal the significance of the metal entity and its interaction with the rod-shaped ceria support in generating oxygen vacancies and Ce^{3+} species. In a similar manner, it was demonstrated that oxygen vacancies and moderate basic sites function as contributing factors in CO_2 activation, with the Ni metal having a pivotal role in H_2 activation and dissociation [100].

Collectively, on the basis of the present results, it can be inferred that Ni is the best metal for methanation reaction, due to its specific d-band center and its ability to activate the CO_2 and H_2 molecules. In this regard, any attempt to optimize the CO_2 hydrogenation performance of Ni-based samples should be focused on the selection of appropriate supporting carriers, and promoters, and fine-tuning engineering approaches towards optimizing the ability of Ni sites (via metal–support interactions) to promote the aforementioned process. In this regard, we recently showed that a compromise between the extent of Ni–ceria perimeter and the competitive presence of larger Ni particles is a prerequisite for maximizing the CO_2 hydrogenation to methane [43]. The latter was ascribed, on the ground of a structure sensitivity analysis, to the presence of highly active edge and kink sites instead of inactive terrace sites. Hence, on the basis of the aforementioned discussion, it could be argued that CO_2 activation could be more favorably promoted on under-coordination sites with an "optimum" d-band center and charge transfer ability.

4. Materials and Methods

4.1. Materials Synthesis

The chemicals used in the present work were $Ce(NO_3)_3{\cdot}6H_2O$ (Acros Organics, Geel, Belgium, purity 99.5%), tetrabutyl titanate (TBOT, Sigma-Aldrich, St. Louis, MO, USA, purity ≥ 97%), NH_4VO_3 (Supelco, Merck, Darmstadt, Germany), $Cr(NO_3)_3{\cdot}9H_2O$ (Sigma-Aldrich, St. Louis, MO, USA, purity 99%), $Mn(NO_3)_2{\cdot}4H_2O$ (Sigma-Aldrich, St. Louis, MO, USA, purity ≥ 97.0%), $Fe(NO_3)_3{\cdot}9H_2O$ (Sigma-Aldrich, St. Louis, MO, USA, purity ≥ 98%), $Co(NO_3)_2{\cdot}6H_2O$ (Sigma-Aldrich, St. Louis, MO, USA, purity ≥ 98%), $Ni(NO_3)_2{\cdot}6H_2O$ (Alfa Aesar, ThermoFisher, Kandel, Germany, purity 98%), $Cu(NO_3)_2{\cdot}3H_2O$ (Sigma-Aldrich, St. Louis, MO, USA, purity 99-104%), $Zn(CH_3COO)_2{\cdot}2H_2O$ (Sigma-Aldrich, St. Louis, MO, USA, purity ≥ 99%) NaOH (Honeywell Fluka, Seelze, Germany, purity ≥ 98%) and ethanol (Supelco, Merck, Darmstadt, Germany).

Bare ceria nanorods (CeO_2-NR) were hydrothermally synthesized, as thoroughly described in our previous work [101]. Ceria-based transition metal samples (TM/CeO_2, TM: Ti, V, Cr, Mn, Fe, Co, Ni, Cu, and Zn) were synthesized by the wet impregnation method, using aqueous solutions of metal nitrate precursors to obtain a nominal metal/cerium atomic ratio of 0.25. The obtained suspensions were heated under stirring until water evaporation, dried at 90 ºC for 12 h, and finally calcined at 500 °C for 2 h (heating ramp 5 °C/min) [44].

4.2. Materials Characterization

The textural properties of samples were assessed by N_2 adsorption–desorption isotherms at −196 °C (Nova 2200e Quantachrome flow apparatus, Boynton Beach, FL, USA). X-ray

diffraction patterns of as-prepared samples were obtained by a Rigaku diffractometer (model RINT 2000, Tokyo, Japan). The crystallite size of the samples was calculated by applying Scherrer's equation (Equation (4)):

$$D_{XRD}(nm) = \frac{K\lambda}{\cos\theta} \quad (4)$$

where λ is the X-ray wavelength in nm, K is Scherrer's constant, B is the line broadening and θ is the Bragg angle. By using Scherrer's equation (Equation (4)), on the most intense diffraction peak, i.e., for CeO_2 (2θ: 28.5°), the primary particle size of this crystal phase was determined. Morphological/elemental analysis was carried out by scanning electron microscopy (SEM, JEOL JSM-6390LV, JEOL Ltd., Akishima, Tokyo, Japan) operating at 20 keV, equipped with an energy dispersive X-ray spectrometry (EDS) system and transmission electron microscopy (TEM) on a JEM-2100 instrument (JEOL, Tokyo, Japan). Temperature Programmed Reduction (H_2-TPR) experiments were carried out in a fully automated AMI-200 Catalyst Characterization Instrument (Altamira Instruments, Pittsburgh, PA, USA) under an H_2 atmosphere, in order to assess the reducibility of the samples. XPS analysis was conducted on Kratos AXIS Ultra HSA, Manchester, United Kingdom with VISION software (http://www.casaxps.com/kratos/, accessed on 10 September 2024) for data acquisition and CASAXPS software (http://www.casaxps.com/, accessed on 10 September 2024) for data analysis.

4.3. Catalytic Evaluation Studies

Catalytic studies were carried out in a quartz fixed-bed U-shaped reactor (i.d. = 1 cm), loaded with 200 mg of catalyst diluted with 200 mg of inert SiO_2. The sample's pre-treatment included in situ reduction at 400 °C for 1 h under pure H_2 flow (40 cm^3 min^{-1}), followed by flushing with He (10 cm^3 min^{-1}) until room temperature. The experiments were conducted at 1 bar and in the temperature range of 200–500 °C at intervals of 15–20 °C and a heating rate of 1 °C/min. The total volumetric feed flow was 100 cm^3 min^{-1}, corresponding to a weight hourly space velocity (WHSV) of 30 $L{\cdot}g^{-1}{\cdot}h^{-1}$. The gas feed constituted a pure H_2/CO_2 mixture at a molar ratio of 80/20. Calculations for the thermodynamic equilibrium were derived using the mathematical model RGibbs in Aspen Plus software (https://www.aspentech.com/en/products/engineering/aspen-plus, accessed on 10 September 2024. Aspen Technology, Inc., Bedford, MA, USA). The analysis of the reactor outlet mixture was performed in a gas chromatograph (Shimadzu GC-14B, Shimadzu, Kyoto, Japan) with He as the carrier gas, equipped with a thermal conductivity detector (TCD) for the detection of CO and CO_2, a flame ionization detector (FID) for monitoring CH_4 and two separation columns (Molecular Sieve 13X, Restek GmbH, Hesse, Germany and Porapak QS, Restek GmbH, Hesse, Germany).

The reactor effluent was passed through a cold trap submerged in an ice bath in order to condensate the H_2O produced by the reactions. The only carbonaceous products detected in the reactor outlet stream were CH_4 and CO. The conversion of carbon dioxide (X_{CO2}), product selectivities (S_{CO} and S_{CH4}), and yields (Y_{CO} and Y_{CH4}) were calculated as follows (Equations (5)–(9)), where [i] stands for the concentration of the respective gas at the outlet of the reactor:

$$X_{CO_2} = 100 \times \frac{[CO] + [CH_4]}{[CO_2] + [CO] + [CH_4]} \quad (5)$$

$$S_{CO} = 100 \times \frac{[CO]}{[CO] + [CH_4]} \quad (6)$$

$$S_{CH_4} = 100 \times \frac{[CH_4]}{[CO] + [CH_4]} \quad (7)$$

$$Y_{CO} = X_{CO_2} \times S_{CO} \quad (8)$$

$$Y_{CH_4} = X_{CH_4} \times S_{CH_4} \quad (9)$$

The macroscopic reaction rates were defined in terms of the rate of moles of CO_2 consumed per mass of the catalyst, r_m;

$$r_m\left(\text{mol } CO_2 \cdot g^{-1} \cdot s^{-1}\right) = \frac{[CO_2]_{in} \times F_{in} \times X_{CO_2}}{100 \times 60 \times m_{cat} \times V_m} \quad (10)$$

where m_{cat} is the mass of the catalyst in grams, and V_m is the gas molar volume at 25 °C and 1 bar (24,436 cm^3/mol).

5. Conclusions

In the present study, a series of TM/CeO_2 catalysts (atomic ratio M/Ce = 0.25) employing the first-row 3d transition metals (Ti, V, Cr, Mn, Fe, Co, Ni, Cu, and Zn) as active metals were catalytically evaluated in CO_2 hydrogenation. The superiority of the Ni/CeO_2 sample was clearly revealed in terms of CO_2 conversion rate and CH_4 selectivity, followed by Co/CeO_2. The 3d early transition metals (Ti–Fe) and the 3d late metals (Cu and Zn) exhibit much lower activity while being selective to CO. The significance of the metal entity in the CO_2 hydrogenation performance was clearly established via a volcano-type dependence of both activity and selectivity to methane as a function of 3d-orbital electron number, with Ni located at the top of this volcano curve. Moreover, a distinct volcano-shaped trend among the relative abundance of oxygen vacancies and Ce^{3+} species with the CO_2 conversion and CH_4 selectivity was disclosed. The present experimental findings agree perfectly with the theoretically predicted trend for CO_2 hydrogenation over 3d transition metals as a function of the energy barrier for CO_2 activation and H_2 dissociation, implying the key role of intrinsic electronic properties of metal entities in conjunction with metal–support interactions rather than of textural/structural characteristics.

Author Contributions: Data curation, formal analysis, investigation, validation, writing—original draft preparation, M.L.; investigation, validation, writing—original draft preparation, S.S.; data curation, investigation, G.V., V.D.B. and G.E.M.; conceptualization, data curation, formal analysis, funding acquisition, project administration, supervision, writing—review and editing, M.K. All authors have read and agreed to the published version of the manuscript.

Funding: This research has been co-financed by the European Union NextGenerationEU under the call RESEARCH–CREATE–INNOVATE 16971 Recovery and Resilience Facility (project code: TAEDK-06169).

Data Availability Statement: The authors confirm that the data supporting the findings of this study are available within the article.

Conflicts of Interest: The authors declare no conflicts of interest.

References

1. Atsbha, T.A.; Yoon, T.; Seongho, P.; Lee, C.-J. A Review on the Catalytic Conversion of CO_2 using H_2 for Synthesis of CO, Methanol, and Hydrocarbons. *J. CO_2 Util.* **2021**, *44*, 101413. [CrossRef]
2. Hansen, J.; Sato, M.; Ruedy, R.; Lo, K.; Lea, D.W.; Medina-Elizade, M. Global temperature change. *Proc. Natl. Acad. Sci. USA* **2006**, *103*, 14288–14293. [CrossRef] [PubMed]
3. Meylan, F.D.; Moreau, V.; Erkman, S. CO_2 Utilization in the Perspective of Industrial Ecology, an Overview. *J. CO_2 Util.* **2015**, *12*, 101–108. [CrossRef]
4. Wang, H.; Liu, Y.; Laaksonen, A.; Krook-Riekkola, A.; Yang, Z.; Lu, X.; Ji, X. Carbon Recycling—An Immense Resource and Key to a Smart Climate Engineering: A Survey of Technologies, Cost and Impurity Impact. *Renew. Sustain. Energy Rev.* **2020**, *131*, 110010. [CrossRef]
5. Saeidi, S.; Amin, N.A.S.; Rahimpour, M.R. Hydrogenation of CO_2 to Value-Added Products—A Review and Potential Future Developments. *J. CO_2 Util.* **2014**, *5*, 66–81. [CrossRef]
6. Bahmanpour, A.M.; Signorile, M.; Kröcher, O. Recent Progress in Syngas Production via Catalytic CO_2 Hydrogenation Reaction. *Appl. Catal. B Environ.* **2021**, *295*, 120319. [CrossRef]
7. Garba, M.D.; Usman, M.; Khan, S.; Shehzad, F.; Galadima, A.; Ehsan, M.F.; Ghanem, A.S.; Humayun, M. CO_2 towards Fuels: A Review of Catalytic Conversion of Carbon Dioxide to Hydrocarbons. *J. Environ. Chem. Eng.* **2021**, *9*, 104756. [CrossRef]

8. Torres-Sempere, G.; Pastor-Perez, L.; Odriozola, J.A.; Yu, J.; Duran-Olivencia, F.J.; Bobadilla, L.F.; Reina, T.R. Recent Advances on Gas-Phase CO_2 Conversion: Catalysis Design and Chemical Processes to Close the Carbon Cycle. *Curr. Opin. Green Sustain. Chem.* **2022**, *36*, 100647. [CrossRef]
9. Rafiee, A.; Rajab Khalilpour, K.; Milani, D.; Panahi, M. Trends in CO_2 Conversion and Utilization: A Review from Process Systems Perspective. *J. Environ. Chem. Eng.* **2018**, *6*, 5771–5794. [CrossRef]
10. Romeo, L.M.; Bailera, M. Design Configurations to Achieve an Effective CO_2 use and Mitigation through Power to Gas. *J. CO_2 Util.* **2020**, *39*, 101174. [CrossRef]
11. Quintino, F.M.; Nascimento, N.; Fernandes, E.C. Aspects of Hydrogen and Biomethane Introduction in Natural Gas Infrastructure and Equipment. *Hydrogen* **2021**, *2*, 301–318. [CrossRef]
12. Konsolakis, M.; Lykaki, M.; Stefa, S.; Carabineiro, S.A.C.; Varvoutis, G.; Papista, E.; Marnellos, G.E. CO_2 Hydrogenation over Nanoceria-Supported Transition Metal Catalysts: Role of Ceria Morphology (Nanorods versus Nanocubes) and Active Phase Nature (Co versus Cu). *Nanomaterials* **2019**, *9*, 1739. [CrossRef] [PubMed]
13. Tawalbeh, M.; Javed, R.M.N.; Al-Othman, A.; Almomani, F. The Novel Contribution of Non-Noble Metal Catalysts for Intensified Carbon Dioxide Hydrogenation: Recent Challenges and Opportunities. *Energy Convers. Manag.* **2023**, *279*, 116755. [CrossRef]
14. Tawalbeh, M.; Javed, R.M.N.; Al-Othman, A.; Almomani, F.; Ajith, S. Unlocking the Potential of CO_2 Hydrogenation into Valuable Products Using Noble Metal Catalysts: A Comprehensive Review. *Environ. Technol. Innov.* **2023**, *31*, 103217. [CrossRef]
15. Ebrahimi, P.; Kumar, A.; Khraisheh, M. A Review of CeO_2 Supported Catalysts for CO_2 Reduction to CO through the Reverse Water Gas Shift Reaction. *Catalysts* **2022**, *12*, 1101. [CrossRef]
16. Chen, X.; Chen, Y.; Song, C.; Ji, P.; Wang, N.; Wang, W.; Cui, L. Recent Advances in Supported Metal Catalysts and Oxide Catalysts for the Reverse Water-Gas Shift Reaction. *Front. Chem.* **2020**, *8*, 709. [CrossRef]
17. Lykaki, M.; Mandela, E.; Varvoutis, G.; Lampropoulos, A.; Marnellos, G.E.; Konsolakis, M. State-of-the-Art Thermocatalytic Systems for CH_4 and CO Production via CO_2 Hydrogenation: Critical Comparison, Mechanistic Considerations and Structure-Performance Insights. *Discov. Chem. Eng.* **2024**, *4*, 11. [CrossRef]
18. Choi, Y.; Sim, G.D.; Jung, U.; Park, Y.; Youn, M.H.; Chun, D.H.; Rhim, G.B.; Kim, K.Y.; Koo, K.Y. Copper Catalysts for CO_2 Hydrogenation to CO through Reverse Water–Gas Shift Reaction for e-Fuel Production: Fundamentals, Recent Advances, and Prospects. *Chem. Eng. J.* **2024**, *492*, 152283. [CrossRef]
19. Gao, X.; Wang, Z.; Huang, Q.; Jiang, M.; Askari, S.; Dewangan, N.; Kawi, S. State-of-Art Modifications of Heterogeneous Catalysts for CO_2 Methanation—Active Sites, Surface Basicity and Oxygen Defects. *Catal. Today* **2022**, *402*, 88–103. [CrossRef]
20. Lee, W.J.; Li, C.; Prajitno, H.; Yoo, J.; Patel, J.; Yang, Y.; Lim, S. Recent Trend in Thermal Catalytic Low Temperature CO_2 Methanation: A Critical Review. *Catal. Today* **2021**, *368*, 2–19. [CrossRef]
21. Ashok, J.; Pati, S.; Hongmanorom, P.; Tianxi, Z.; Junmei, C.; Kawi, S. A Review of Recent Catalyst Advances in CO_2 Methanation Processes. *Catal. Today* **2020**, *356*, 471–489. [CrossRef]
22. Memon, M.A.; Jiang, Y.; Hassan, M.A.; Ajmal, M.; Wang, H.; Liu, Y. Heterogeneous Catalysts for Carbon Dioxide Methanation: A View on Catalytic Performance. *Catalysts* **2023**, *13*, 1514. [CrossRef]
23. Bacariza, M.C.; Spataru, D.; Karam, L.; Lopes, J.M.; Henriques, C. Promising Catalytic Systems for CO_2 Hydrogenation into CH_4: A Review of Recent Studies. *Processes* **2020**, *8*, 1646. [CrossRef]
24. Hussain, I.; Tanimu, G.; Ahmed, S.; Aniz, C.U.; Alasiri, H.; Alhooshani, K. A Review of the Indispensable Role of Oxygen Vacancies for Enhanced CO_2 Methanation Activity over CeO_2-Based Catalysts: Uncovering, Influencing, and Tuning Strategies. *Int. J. Hydrog. Energy* **2023**, *48*, 24663–24696. [CrossRef]
25. Konsolakis, M.; Lykaki, M. Facet-Dependent Reactivity of Ceria Nanoparticles Exemplified by CeO_2-Based Transition Metal Catalysts: A Critical Review. *Catalysts* **2021**, *11*, 452. [CrossRef]
26. Yang, C.; Lu, Y.; Zhang, L.; Kong, Z.; Yang, T.; Tao, L.; Zou, Y.; Wang, S. Defect Engineering on CeO_2-Based Catalysts for Heterogeneous Catalytic Applications. *Small Struct.* **2021**, *2*, 2100058. [CrossRef]
27. Manan, W.N.; Wan Isahak, W.N.R.; Yaakob, Z. CeO_2-Based Heterogeneous Catalysts in Dry Reforming Methane and Steam Reforming Methane: A Short Review. *Catalysts* **2022**, *12*, 452. [CrossRef]
28. Dong, C.; Zong, X.; Jiang, W.; Niu, L.; Liu, Z.; Qu, D.; Wang, X.; Sun, Z. Recent Advances of Ceria-Based Materials in the Oxidation of Carbon Monoxide. *Small Struct.* **2021**, *2*, 2000081. [CrossRef]
29. Fan, L.; Zhang, J.; Ma, K.; Zhang, Y.; Hu, Y.-M.; Kong, L.; Jia, A.; Zhang, Z.; Huang, W.; Lu, J.-Q. Ceria Morphology-Dependent Pd-CeO_2 Interaction and Catalysis in CO_2 Hydrogenation into Formate. *J. Catal.* **2021**, *397*, 116–127. [CrossRef]
30. Jiang, F.; Wang, S.; Liu, B.; Liu, J.; Wang, L.; Xiao, Y.; Xu, Y.; Liu, X. Insights into the Influence of CeO_2 Crystal Facet on CO_2 Hydrogenation to Methanol over Pd/CeO_2 Catalysts. *ACS Catal.* **2020**, *10*, 11493–11509. [CrossRef]
31. Martin, N.M.; Velin, P.; Skoglundh, M.; Bauer, M.; Carlsson, P.-A. Catalytic Hydrogenation of CO_2 to Methane over Supported Pd, Rh and Ni Catalysts. *Catal. Sci. Technol.* **2017**, *7*, 1086–1094. [CrossRef]
32. Khobragade, R.; Roškarič, M.; Žerjav, G.; Košiček, M.; Zavašnik, J.; Van de Velde, N.; Jerman, I.; Tušar, N.N.; Pintar, A. Exploring the Effect of Morphology and Surface Properties of Nanoshaped Pd/CeO_2 Catalysts on CO_2 Hydrogenation to Methanol. *Appl. Catal. A Gen.* **2021**, *627*, 118394. [CrossRef]
33. Wang, C.; Lu, Y.; Zhang, Y.; Fu, H.; Sun, S.; Li, F.; Duan, Z.; Liu, Z.; Wu, C.; Wang, Y.; et al. Ru-Based Catalysts for Efficient CO_2 Methanation: Synergistic Catalysis between Oxygen Vacancies and Basic Sites. *Nano Res.* **2023**, *16*, 12153–12164. [CrossRef]

34. Chen, M.; Liu, L.; Chen, X.; Qin, X.; Li, K.; Zhang, J.; Bao, X.; Ma, L.; Zhang, C. Effects of Ru Particle Size over TiO_2 on the Catalytic Performance of CO_2 Hydrogenation. *Appl. Surf. Sci.* **2024**, *654*, 159640. [CrossRef]
35. Akter, N.; Zhang, S.; Lee, J.; Kim, D.H.; Boscoboinik, J.A.; Kim, T. Selective Catalytic Reduction of NO by Ammonia and NO Oxidation Over CoO_x/CeO_2 Catalysts. *Mol. Catal.* **2020**, *482*, 110664. [CrossRef]
36. Bian, Z.; Chan, Y.M.; Yu, Y.; Kawi, S. Morphology Dependence of Catalytic Properties of Ni/CeO_2 for CO_2 Methanation: A Kinetic and Mechanism Study. *Catal. Today* **2020**, *347*, 31–38. [CrossRef]
37. Konsolakis, M.; Lykaki, M. Recent Advances on the Rational Design of Non-Precious Metal Oxide Catalysts Exemplified by CuO_x/CeO_2 Binary System: Implications of Size, Shape and Electronic Effects on Intrinsic Reactivity and Metal-Support Interactions. *Catalysts* **2020**, *10*, 160. [CrossRef]
38. Xiao, M.; Zhang, X.; Yang, Y.; Cui, X.; Chen, T.; Wang, Y. M (M = Mn, Co, Cu)-CeO_2 Catalysts to Enhance Their CO Catalytic Oxidation at a Low Temperature: Synergistic Effects of the Interaction between Ce^{3+}-M^{x+}-Ce^{4+} and the Oxygen Vacancy Defects. *Fuel* **2022**, *323*, 124379. [CrossRef]
39. Cargnello, M.; Fornasiero, P.; Gorte, R.J. Opportunities for Tailoring Catalytic Properties through Metal-Support Interactions. *Catal. Lett.* **2012**, *142*, 1043–1048. [CrossRef]
40. Liu, C.; Cundari, T.R.; Wilson, A.K. CO_2 Reduction on Transition Metal (Fe, Co, Ni, and Cu) Surfaces: In Comparison with Homogeneous Catalysis. *J. Phys. Chem. C* **2012**, *116*, 5681–5688. [CrossRef]
41. Li, Y.; Zhang, X.; Zheng, Z. A Review of Transition Metal Oxygen-Evolving Catalysts Decorated by Cerium-Based Materials: Current Status and Future Prospects. *CCS Chem.* **2022**, *4*, 31–53. [CrossRef]
42. Varvoutis, G.; Lykaki, M.; Marnellos, G.E.; Konsolakis, M. Recent Advances on Fine-Tuning Engineering Strategies of CeO_2-Based Nanostructured Catalysts Exemplified by CO_2 Hydrogenation Processes. *Catalysts* **2023**, *13*, 275. [CrossRef]
43. Varvoutis, G.; Lykaki, M.; Stefa, S.; Binas, V.; Marnellos, G.E.; Konsolakis, M. Deciphering the Role of Ni Particle Size and Nickel-Ceria Interfacial Perimeter in the Low-Temperature CO_2 Methanation Reaction over Remarkably Active Ni/CeO_2 Nanorods. *Appl. Catal. B Environ.* **2021**, *297*, 120401. [CrossRef]
44. Varvoutis, G.; Lykaki, M.; Stefa, S.; Papista, E.; Carabineiro, S.A.C.; Marnellos, G.E.; Konsolakis, M. Remarkable Efficiency of Ni Supported on Hydrothermally Synthesized CeO_2 Nanorods for Low-Temperature CO_2 Hydrogenation to Methane. *Catal. Commun.* **2020**, *142*, 106036. [CrossRef]
45. Podrojková, N.; Sans, V.; Oriňak, A.; Oriňaková, R. Recent Developments in the Modelling of Heterogeneous Catalysts for CO_2 Conversion to Chemicals. *ChemCatChem* **2020**, *12*, 1802–1825. [CrossRef]
46. Jangam, A.; Das, S.; Dewangan, N.; Hongmanorom, P.; Hui, W.M.; Kawi, S. Conversion of CO_2 to C_1 Chemicals: Catalyst Design, Kinetics and Mechanism Aspects of the Reactions. *Catal. Today* **2020**, *358*, 3–29. [CrossRef]
47. Saeidi, S.; Najari, S.; Fazlollahi, F.; Nikoo, M.K.; Sefidkon, F.; Klemeš, J.J.; Baxter, L.L. Mechanisms and Kinetics of CO_2 Hydrogenation to Value-Added Products: A Detailed Review on Current Status and Future Trends. *Renew. Sustain. Energy Rev.* **2017**, *80*, 1292–1311. [CrossRef]
48. Su, X.; Yang, X.; Zhao, B.; Huang, Y. Designing of Highly Selective and High-Temperature Endurable RWGS Heterogeneous Catalysts: Recent Advances and the Future Directions. *J. Energy Chem.* **2017**, *26*, 854–867. [CrossRef]
49. Zhang, W.; Sun, J.; Wang, H.; Cui, X. Recent Advances in Hydrogenation of CO_2 to CO with Heterogeneous Catalysts Through the RWGS Reaction. *Chem. Asian J.* **2024**, *19*, e202300971. [CrossRef]
50. Triviño, M.L.T.; Arriola, N.C., Jr.; Seok Kang, Y.; Gil Seo, J. Transforming CO_2 to Valuable Feedstocks: Emerging Catalytic and Technological Advances for the Reverse Water Gas Shift Reaction. *Chem. Eng. J.* **2024**, *487*, 150369. [CrossRef]
51. Xie, Y.; Wen, J.; Li, Z.; Chen, J.; Zhang, Q.; Ning, P.; Chen, Y.; Hao, J. Progress in Reaction Mechanisms and Catalyst Development of Ceria-Based Catalysts for Low-Temperature CO_2 Methanation. *Green Chem.* **2023**, *25*, 130–152. [CrossRef]
52. Alam, M.I.; Cheula, R.; Moroni, G.; Nardi, L.; Maestri, M. Mechanistic and Multiscale Aspects of Thermo-Catalytic CO_2 conversion to C_1 products. *Catal. Sci. Technol.* **2021**, *11*, 6601–6629. [CrossRef] [PubMed]
53. Gao, X.; Cai, P.; Wang, Z.; Lv, X.; Kawi, S. Surface Acidity/Basicity and Oxygen Defects of Metal Oxide: Impacts on Catalytic Performances of CO_2 Reforming and Hydrogenation Reactions. *Top. Catal.* **2023**, *66*, 299–325. [CrossRef]
54. Etim, U.J.; Zhang, C.; Zhong, Z. Impacts of the Catalyst Structures on CO_2 Activation on Catalyst Surfaces. *Nanomaterials* **2021**, *11*, 3265. [CrossRef] [PubMed]
55. Ray, K.; Deo, G. A Potential Descriptor for the CO_2 Hydrogenation to CH_4 over Al_2O_3 Supported Ni and Ni-Based Alloy Catalysts. *Appl. Catal. B Environ.* **2017**, *218*, 525–537. [CrossRef]
56. Feibelman, P.J.; Hamann, D.R. Electronic Structure of a "Poisoned" Transition-Metal Surface. *Phys. Rev. Lett.* **1984**, *52*, 61–64. [CrossRef]
57. Escaño, M.C.; Nguyen, T.Q.; Nakanishi, H.; Kasai, H. Another way of looking at bonding on bimetallic surfaces: The role of spin polarization of surface metal d states. *J. Phys. Condens. Matter* **2009**, *21*, 492201. [CrossRef]
58. Sun, J.; Zhao, H.; Fang, X.; Zhai, S.; Zhai, D.; Sun, L.; Deng, W. Theoretical Studies on the Catalytic Hydrogenation of Carbon Dioxide by 3d Transition Metals Single-Atom Catalyst Supported on Covalent Triazine Frameworks. *Mol. Catal.* **2021**, *508*, 111581. [CrossRef]
59. Sebastian, R.; Swapna, M.S.; Sankararaman, S. Thermal Lens Study of Absolute Porosity in Ceria: A Sankar–Loeb Model Approach. *SN Appl. Sci.* **2020**, *2*, 1145. [CrossRef]

60. Deori, K.; Gupta, D.; Saha, B.; Awasthi, S.K.; Deka, S. Introducing Nanocrystalline CeO_2 as Heterogeneous Environmental Friendly Catalyst for the Aerobic Oxidation of Para-Xylene to Terephthalic Acid in Water. *J. Mater. Chem. A* **2013**, *1*, 7091–7099. [CrossRef]
61. Peyrovi, P.; Gillot, S.; Dacquin, J.-P.; Granger, P.; Dujardin, C. The Activity of $CeVO_4$-Based Catalysts for Ammonia-SCR: Impact of Surface Cerium Enrichment. *Catal. Lett.* **2021**, *151*, 1003–1012. [CrossRef]
62. Mosleh, M.; Mahinpour, A. Sonochemical Synthesis and Characterization of Cerium Vanadate Nanoparticles and Investigation of Its Photocatalyst Application. *J. Mater. Sci. Mater. Electron.* **2016**, *27*, 8930–8934. [CrossRef]
63. Rao, G.R. Influence of Metal Particles on the Reduction Properties of Ceria-Based Materials Studied by TPR. *Bull. Mater. Sci.* **1999**, *22*, 89–94. [CrossRef]
64. Kammert, J.; Moon, J.; Wu, Z. A Review of the Interactions between Ceria and H_2 and the Applications to Selective Hydrogenation of Alkynes. *Chin. J. Catal.* **2020**, *41*, 901–914. [CrossRef]
65. Sudarsanam, P.; Hillary, B.; Amin, M.H.; Rockstroh, N.; Bentrup, U.; Brückner, A.; Bhargava, S.K. Heterostructured Copper-Ceria and Iron-Ceria Nanorods: Role of Morphology, Redox, and Acid Properties in Catalytic Diesel Soot Combustion. *Langmuir* **2018**, *34*, 2663–2673. [CrossRef] [PubMed]
66. Bayram, B.; Soykal, I.I.; Von Deak, D.; Miller, J.T.; Ozkan, U.S. Ethanol Steam Reforming over Co-Based Catalysts: Investigation of Cobalt Coordination Environment under Reaction Conditions. *J. Catal.* **2011**, *284*, 77–89. [CrossRef]
67. Guo, X.; Zhou, R. A New Insight into the Morphology Effect of Ceria on CuO/CeO_2 Catalysts for CO Selective Oxidation in Hydrogen-Rich Gas. *Catal. Sci. Technol.* **2016**, *6*, 3862–3871. [CrossRef]
68. Liu, H.-X.; Li, S.-Q.; Wang, W.-W.; Yu, W.-Z.; Zhang, W.-J.; Ma, C.; Jia, C.-J. Partially Sintered Copper–ceria as Excellent Catalyst for the High-Temperature Reverse Water Gas Shift Reaction. *Nat. Commun.* **2022**, *13*, 867. [CrossRef]
69. Oo, W.; Park, J.H.; Sonia, Z.A.; Win, M.Z.; Cho, D.; Yi, K.B. Modification of Copper-Ceria Catalyst via Reverse Microemulsion Method and Study of the Effects of Surfactant on WGS Catalyst Activity. *Catalysts* **2023**, *13*, 951. [CrossRef]
70. Zhao, P.; Qin, F.; Huang, Z.; Sun, C.; Shen, W.; Xu, H. Morphology-Dependent Oxygen Vacancies and Synergistic Effects of Ni/CeO_2 Catalysts for N_2O Decomposition. *Catal. Sci. Technol.* **2018**, *8*, 276–288. [CrossRef]
71. Serafin, J.; Llorca, J. Nanoshaped Cerium Oxide with Nickel as a Non-Noble Metal Catalyst for CO_2 Thermochemical Reactions. *Molecules* **2023**, *28*, 2926. [CrossRef] [PubMed]
72. Zhang, F.; Wang, P.; Koberstein, J.; Khalid, S.; Chan, S.-W. Cerium Oxidation State in Ceria Nanoparticles Studied with X-Ray Photoelectron Spectroscopy and Absorption near Edge Spectroscopy. *Surf. Sci.* **2004**, *563*, 74–82. [CrossRef]
73. Sohn, H.; Celik, G.; Gunduz, S.; Dogu, D.; Zhang, S.; Shan, J.; Tao, F.F.; Ozkan, U.S. Oxygen Mobility in Pre-Reduced Nano- and Macro-Ceria with Co Loading: An AP-XPS, In-Situ DRIFTS and TPR Study. *Catal. Lett.* **2017**, *147*, 2863–2876. [CrossRef]
74. Xu, J.; Harmer, J.; Li, G.; Chapman, T.; Collier, P.; Longworth, S.; Tsang, S.C. Size Dependent Oxygen Buffering Capacity of Ceria Nanocrystals. *Chem. Commun.* **2010**, *46*, 1887–1889. [CrossRef]
75. Alkhoori, A.A.; Elmutasim, O.; Dabbawala, A.A.; Vasiliades, M.A.; Petallidou, K.C.; Emwas, A.-H.; Anjum, D.H.; Singh, N.; Baker, M.A.; Charisiou, N.D.; et al. Mechanistic Features of the CeO_2-Modified Ni/Al_2O_3 Catalysts for the CO_2 Methanation Reaction: Experimental and Ab Initio Studies. *ACS Appl. Energy Mater.* **2023**, *6*, 8550–8571. [CrossRef]
76. Szamosvölgyi, Á.; Rajkumar, T.; Sápi, A.; Szenti, I.; Ábel, M.; Gómez-Pérez, J.F.; Baán, K.; Fogarassy, Z.; Dodony, E.; Pécz, B.; et al. Interfacial Ni Active Sites Strike Solid Solutional Counterpart in CO_2 Hydrogenation. *Environ. Technol. Innov.* **2022**, *27*, 102747. [CrossRef]
77. Kuan, W.-F.; Chung, C.-H.; Lin, M.M.; Tu, F.-Y.; Chen, Y.-H.; Yu, W.-Y. Activation of Carbon Dioxide with Surface Oxygen Vacancy of Ceria Catalyst: An Insight from in-Situ X-Ray Absorption near Edge Structure Analysis. *Mater. Today Sustain.* **2023**, *23*, 100425. [CrossRef]
78. Martin, N.M.; Hemmingsson, F.; Schaefer, A.; Ek, M.; Merte, L.R.; Hejral, U.; Gustafson, J.; Skoglundh, M.; Dippel, A.-C.; Gutowski, O.; et al. Structure-Function Relationship for CO_2 Methanation over Ceria Supported Rh and Ni Catalysts under Atmospheric Pressure Conditions. *Catal. Sci. Technol.* **2019**, *9*, 1644–1653. [CrossRef]
79. Cao, F.; Xiao, Y.; Zhang, Z.; Li, J.; Xia, Z.; Hu, X.; Ma, Y.; Qu, Y. Influence of Oxygen Vacancies of CeO_2 on Reverse Water Gas Shift Reaction. *J. Catal.* **2022**, *414*, 25–32. [CrossRef]
80. Jenkinson, K.; Spadaro, M.C.; Golovanova, V.; Andreu, T.; Morante, J.R.; Arbiol, J.; Bals, S. Direct Operando Visualization of Metal Support Interactions Induced by Hydrogen Spillover During CO_2 Hydrogenation. *Adv. Mater.* **2023**, *35*, 2306447. [CrossRef]
81. Ye, H.; Na, W.; Gao, W.; Wang, H. Carbon-Modified CuO/ZnO Catalyst with High Oxygen Vacancy for CO_2 Hydrogenation to Methanol. *Energy Technol.* **2020**, *8*, 2000194. [CrossRef]
82. Jiang, D.; Wang, W.; Zhang, L.; Zheng, Y.; Wang, Z. Insights into the Surface-Defect Dependence of Photoreactivity over CeO_2 Nanocrystals with Well-Defined Crystal Facets. *ACS Catal.* **2015**, *5*, 4851–4858. [CrossRef]
83. Hu, J.; Wei, F.; Hu, X.; Xu, J.; Deng, W. Synthesis of CuO-Loaded Ceria Hollow Spheres for Catalytic CO Oxidation. *ChemistrySelect* **2022**, *7*, e202103476. [CrossRef]
84. Konsolakis, M.; Sgourakis, M.; Carabineiro, S.A.C. Surface and Redox Properties of Cobalt-Ceria Binary Oxides: On the Effect of Co Content and Pretreatment Conditions. *Appl. Surf. Sci.* **2015**, *341*, 48–54. [CrossRef]
85. Zhan, Y.; Liu, Y.; Peng, X.; Zhao, W.; Zhang, Y.; Wang, X.; Au, C.; Jiang, L. Molecular-Level Understanding of Reaction Path Optimization as a Function of Shape Concerning the Metal-Support Interaction Effect of Co/CeO_2 on Water-Gas Shift Catalysis. *Catal. Sci. Technol.* **2019**, *9*, 4928–4937. [CrossRef]

86. Lykaki, M.; Stefa, S.; Carabineiro, S.A.C.; Pandis, P.K.; Stathopoulos, V.N.; Konsolakis, M. Facet-Dependent Reactivity of Fe_2O_3/CeO_2 Nanocomposites: Effect of Ceria Morphology on CO Oxidation. *Catalysts* **2019**, *9*, 371. [CrossRef]
87. Yogendra, K.; Sitaramulu, P.; Nazeer, S.; Kumar, P.M.; Reddy, B.M.; Rao, T.V. Influence of Iron Doping in Mesoporous Ceria on the Physicochemical Properties and Catalytic Activity in Styrene Oxidation. *Appl. Surf. Sci.* **2024**, *676*, 160971. [CrossRef]
88. Wang, H.; Jin, B.; Wang, H.; Ma, N.; Liu, W.; Weng, D.; Wu, X.; Liu, S. Study of Ag Promoted Fe_2O_3@CeO_2 as Superior Soot Oxidation Catalysts: The Role of Fe_2O_3 Crystal Plane and Tandem Oxygen Delivery. *Appl. Catal. B Environ.* **2018**, *237*, 251–262. [CrossRef]
89. Liu, F.; Wang, Z.; Wang, D.; Chen, D.; Chen, F.; Li, X. Morphology and Crystal-Plane Effects of Fe/W-CeO_2 for Selective Catalytic Reduction of NO with NH_3. *Catalysts* **2019**, *9*, 288. [CrossRef]
90. Liu, W.; Wang, W.; Tang, K.; Guo, J.; Ren, Y.; Wang, S.; Feng, L.; Yang, Y. The Promoting Influence of Nickel Species in the Controllable Synthesis and Catalytic Properties of Nickel-Ceria Catalysts. *Catal. Sci. Technol.* **2016**, *6*, 2427–2434. [CrossRef]
91. Tang, K.; Liu, W.; Li, J.; Guo, J.; Zhang, J.; Wang, S.; Niu, S.; Yang, Y. The Effect of Exposed Facets of Ceria to the Nickel Species in Nickel-Ceria Catalysts and Their Performance in a NO + CO Reaction. *ACS Appl. Mater. Interfaces* **2015**, *7*, 26839–26849. [CrossRef] [PubMed]
92. Musab Ahmed, S.; Ren, J.; Ullah, I.; Lou, H.; Xu, N.; Abbasi, Z.; Wang, Z. Ni-Based Catalysts for CO_2 Methanation: Exploring the Support Role in Structure-Activity Relationships. *ChemSusChem* **2024**, *17*, e202400310. [CrossRef] [PubMed]
93. Boaro, M.; Colussi, S.; Trovarelli, A. Ceria-Based Materials in Hydrogenation and Reforming Reactions for CO_2 Valorization. *Front. Chem.* **2019**, *7*, 28. [CrossRef] [PubMed]
94. Liu, Y.; Li, D.; Zhao, H.; Wang, C.; Xu, Y.; Li, L.; Li, Z.; Wang, H.; Li, K. Boosting CO_2 Methanation Activity by Tuning Ni Crystal Plane and Oxygen Vacancy in Ni/CeO_2 Catalyst. *Chem. Eng. J.* **2024**, *494*, 153004. [CrossRef]
95. Dietz, L.; Piccinin, S.; Maestri, M. Mechanistic Insights into CO_2 Activation via Reverse Water—Gas Shift on Metal Surfaces. *J. Phys. Chem. C* **2015**, *119*, 4959–4966. [CrossRef]
96. Wang, S.-G.; Liao, X.-Y.; Cao, D.-B.; Huo, C.-F.; Li, Y.-W.; Wang, J.; Jiao, H. Factors Controlling the Interaction of CO_2 with Transition Metal Surfaces. *J. Phys. Chem. C* **2007**, *111*, 16934–16940. [CrossRef]
97. Bhattacharjee, S.; Waghmare, U.V.; Lee, S.-C. An improved d-band model of the catalytic activity of magnetic transition metal surfaces. *Sci. Rep.* **2016**, *6*, 35916. [CrossRef]
98. Lee, S.M.; Lee, Y.H.; Moon, D.H.; Ahn, J.Y.; Nguyen, D.D.; Chang, S.W.; Kim, S.S. Reaction Mechanism and Catalytic Impact of Ni/CeO_{2-X} Catalyst for Low-Temperature CO_2 Methanation. *Ind. Eng. Chem. Res.* **2019**, *58*, 8656–8662. [CrossRef]
99. Huang, W.; Gao, Y. Morphology-Dependent Surface Chemistry and Catalysis of CeO_2 Nanocrystals. *Catal. Sci. Technol.* **2014**, *4*, 3772–3784. [CrossRef]
100. Li, L.; Jiang, L.; Li, D.; Yuan, J.; Bao, G.; Li, K. Enhanced Low-Temperature Activity of CO_2 Methanation over Ni/CeO_2 Catalyst: Influence of Preparation Methods. *Appl. Catal. O Open* **2024**, *192*, 206956. [CrossRef]
101. Lykaki, M.; Pachatouridou, E.; Carabineiro, S.A.C.; Iliopoulou, E.; Andriopoulou, C.; Kallithrakas-Kontos, N.; Boghosian, S.; Konsolakis, M. Ceria nanoparticles shape effects on the structural defects and surface chemistry: Implications in CO oxidation by Cu/CeO_2 catalysts. *Appl. Catal. B Environ.* **2018**, *230*, 18–28. [CrossRef]

Disclaimer/Publisher's Note: The statements, opinions and data contained in all publications are solely those of the individual author(s) and contributor(s) and not of MDPI and/or the editor(s). MDPI and/or the editor(s) disclaim responsibility for any injury to people or property resulting from any ideas, methods, instructions or products referred to in the content.